



Published in final edited form as:

Dalton Trans. 2015 November 7; 44(41): 18111–18121. doi:10.1039/c5dt02138c.

¹⁹F NMR Study of Ligand Dynamics in Carboxylate-Bridged Diiron(II) Complexes Supported by a Macrocyclic Ligand

Mikael A. Minier and Stephen J. Lippard

Department of Chemistry, Massachusetts Institute of Technology, Cambridge, MA 02139

Abstract

A series of asymmetrically carboxylate-bridged diiron(II) complexes featuring fluorine atoms as NMR spectroscopic probes, [Fe₂(PIM)(Ar^{4F-Ph}CO₂)₂] (**10**), [Fe₂(F₂PIM)(Ar^{Tol}CO₂)₂] (**11**), and [Fe₂(F₂PIM)(Ar^{4F-Ph}CO₂)₂] (**12**), were prepared and characterized by X-ray crystallography, Mössbauer spectroscopy, and VT ¹⁹F NMR spectroscopy. These complexes are part of a rare family of syn-*N* diiron(II) complexes, [Fe₂(X₂PIM)(RCO₂)₂], that are structurally very similar to the active site of the hydroxylase enzyme component of reduced methane monooxygenase (MMOH_{red}). Solution characterization of these complexes demonstrates that they undergo intramolecular carboxylate rearrangements, or carboxylate shifts, a dynamic feature relevant to the reactivity of the diiron centers in bacterial multicomponent monooxygenases.

Keywords

Diiron; biomimetic; carboxylate; fluorine NMR; X-ray structure; iron; macrocycle

Introduction

Biology utilizes enzymes with carboxylate-bridged diiron centers to catalyze difficult transformations such as methane oxidation by methane monooxygenase (MMO).^{1–4} These diiron centers typically have an asymmetric arrangement of ligands that is conserved across the superfamily of bacterial multicomponent monooxygenases (BMMs) (Figure 1).^{5–8} In general, two nitrogen donors from histidine bind to the diiron unit in a syn fashion with respect to the diiron vector. The bridging carboxylates adopt different coordination modes. In the reduced state of the MMO hydroxylase component (MMOH_{red}), one carboxylate bridges in a symmetric $\mu\text{-}\eta^1:\eta^1$ fashion and the other in an asymmetric $\mu\text{-}\eta^1:\eta^2$ mode. In the oxidized form of the enzyme, MMOH_{ox}, the latter carboxylate shifts into a monodentate terminal position. This alteration in the carboxylate bridging mode, or carboxylate shift,⁹ is proposed to be mechanistically important based on both biological⁴ and synthetic model studies^{10,11} (Scheme 1).

^{*}To whom correspondence should be addressed. lippard@mit.edu.

Supporting Information

X-ray crystallographic data, Mössbauer spectra, and NMR spectra. This material is available free of charge via the Internet at <http://pubs.acs.org>.

Efforts to replicate the chemistry of MMOH using small molecules have been reviewed.^{12,13} The rational synthesis of carboxylate-bridged dinuclear metal complexes is challenging, owing to the propensity of these ligands to form polymers. Reliable strategies involve the use of sterically demanding ligands such as *m*-terphenyl carboxylates or dinucleating ligand frameworks. A variety of binding modes are possible for carboxylate-bridged diiron complexes. In the solid state structure of $[\text{LFe}_2(\text{OAc}_3)] \cdot 2\text{MeCN}$, where L is a bis-tetradentate pyrazolate, all carboxylate binding modes in a dinuclear system were observed within two molecules in the asymmetric unit in the crystals.¹⁴ Moreover, the solution structures of these complexes may differ from those in the solid or may switch between multiple conformations. For example, ¹⁹F NMR spectroscopic studies of $[\text{Fe}_2(\text{Ar}^{4\text{F-Ph}}\text{CO}_2)_4(\text{THF})_2]$ ($\text{Ar}^{4\text{F-Ph}} = 2,6\text{-bis-4-fluorophenylphenyl}$) revealed an equilibrium between doubly and quadruply bridged forms, with conversion to the quadruply bridged form below -60°C .¹⁵

Previously, our lab reported two diiron(II) complexes, $[\text{Fe}_2(\text{PIM})(\text{Ph}_3\text{CCO}_2)_2]$ (**1**) and $[\text{Fe}_2(\text{PIM})(\text{Ar}^{\text{Tol}}\text{CO}_2)_2]$ (**2**) ($\text{Ar}^{\text{Tol}} = 2,6\text{-bis-tolylphenyl}$), supported by the dinucleating macrocyclic ligand, H_2PIM (Scheme 2, inset).¹⁶ Together with bulky carboxylate ligands, the PIM^{2-} macrocycle enforces geometries in diiron(II) complexes featuring syn-*N* coordination and asymmetric carboxylate bridging modes, closely resembling that in MMOH_{red} . Complexes **1** and **2** were characterized by X-ray crystallography, Mössbauer spectroscopy, UV-Vis, EPR, and NMR spectroscopy, and by cyclic voltammetry. Reaction of **2** with AgClO_4 produced the diiron(III) complex, $[\text{Fe}_2(\mu\text{-OH})_2(\text{ClO}_4)_2(\text{PIM})(\text{Ar}^{\text{Tol}}\text{CO}_2)\text{Ag}]$ (**3**), and reaction of **2** with AgSbF_6 formed a species believed to be the tetrairon(III) complex, $[\text{Fe}_4(\mu\text{-F})_6(\text{PIM})_2(\text{Ar}^{\text{Tol}}\text{CO}_2)_2]$, which was not fully characterized. When **1** was allowed to react with O_2 , three iron(III) species were observed, two of which were identified as $[\text{Fe}_2(\mu\text{-OH})(\text{PIM})(\text{Ph}_3\text{CCO}_2)_3]$ (**4**) and $[\text{Fe}_4(\mu\text{-OH})_6(\text{PIM})_2(\text{Ph}_3\text{CCO}_2)_2]$ (**5**). The reaction of **2** with O_2 produced a mixture of $[\text{Fe}_2(\mu\text{-O})(\text{PIM})(\text{Ar}^{\text{Tol}}\text{CO}_2)_2]$ (**6**) and $[\text{Fe}_2(\mu\text{-OH})_2(\text{PIM})(\text{Ar}^{\text{Tol}}\text{CO}_2)_2]$ (**7**), complexes that resemble the resting diiron(III) state, MMOH_{ox} , of MMO. When **6/7** further reacted with water, $[\text{Fe}_4(\mu\text{-OH})_6(\text{PIM})_2(\text{Ar}^{\text{Tol}}\text{CO}_2)_2]$ (**8**) formed.

With rare syn-*N* asymmetrically carboxylate-bridged diiron(II) complexes **1–2** in hand, we sought to understand their solution dynamics by applying NMR spectroscopy. Because of their paramagnetism, however, **1** and **2** are not well suited for such a study. We therefore introduced fluorine atoms as ¹⁹F NMR spectroscopic handles by modifying the macrocyclic H_2PIM ligand to create $\text{H}_2\text{F}_2\text{PIM}$, and introduced the fluorinated terphenylcarboxylate, $\text{Ar}^{4\text{FPh}}\text{CO}_2\text{H}$, which we used previously to investigate the dynamics of the diiron(II) tetracarboxylate complexes as mentioned above. With these ligands, we prepared three new diiron(II) complexes, $[\text{Fe}_2(\text{PIM})(\text{Ar}^{4\text{F-Ph}}\text{CO}_2)_2]$ (**10**), $[\text{Fe}_2(\text{F}_2\text{PIM})(\text{Ar}^{\text{Tol}}\text{CO}_2)_2]$ (**11**), and $[\text{Fe}_2(\text{F}_2\text{PIM})(\text{Ar}^{4\text{F-Ph}}\text{CO}_2)_2]$ (**12**). Their solution dynamics were probed by using VT ¹⁹F NMR spectroscopy.

Experimental Methods

General Considerations

Chemicals were purchased from commercial sources and used as received. Solvents were saturated with argon, purified by the passage through two columns of activated alumina, and stored over 3 Å molecular sieves in an MBraun dry box. (2-Hydroxy-5-methylphenyl)boronic acid, (2-hydroxy-5-fluorophenyl)boronic acid, H₂PIM, Ar^{Tol}CO₂H, Ar^{4FPh}CO₂H, compounds **L4a**, and **2**, were prepared according to published procedures.^{17,18,16} All manipulations of air sensitive compounds were performed in an MBraun dry box. A Thermo Nicolet Avatar 360 spectrometer was used to obtain IR spectra and the data were processed with the OMNIC software. Melting points were obtained with a Stanford Research Systems OptiMelt. NMR spectra were recorded on either a 500 MHz Varian Inova spectrometer or a 300 MHz Varian Mercury spectrometer. ¹H and ¹³C spectra were referenced to residual solvent peaks. ¹⁹F spectra were referenced to CFC1₃ (0.00 ppm). VT-NMR between 308 and 178 K were performed on a 500 MHz Varian Inova spectrometer. Reversibility of the VT-NMR experiments was confirmed by comparing initial and final spectra at room temperature. ⁵⁷Fe Mössbauer spectra were obtained on a WEB Research Co. MSI spectrometer with a ⁵⁷Co source in Rh matrix. Solid samples were pulverized and suspended in Apiezon M grease inside a nylon sample holder and corresponding spectra were obtained at 80 K. Isomer shift values (δ) were referenced to metallic iron foil and spectra were fit to Lorentzian lines using the WMOSS program.

X-Ray Data Collection and Refinement

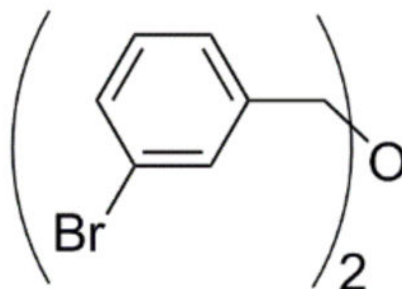
Single crystals of H₂PIM, H₂F₂PIM, and **10–12**, were coated with Paratone oil and mounted onto a Bruker SMART APEX CCD X-ray diffractometer using Mo K α radiation. Data collection was performed at 100 K and the diffractometer was controlled with the APEX2 (v. 2010.1–2) software package.¹⁹ Data reduction was performed with SAINT²⁰ and absorption corrections with SADABS.²¹ XPREP²² was used to determine the space group through analysis of metric symmetry and systematic absences. Initial solutions were determined using direct methods and refinement was performed with either the SHELXL-97 software package or SHELX-2014 using full-matrix least squares refinement on F².²³ PLATON²⁴ was used to check for higher symmetry. Non-hydrogen atoms were refined anisotropically. Hydrogen atoms were fixed at idealized positions using a riding model except for the hydroxyl protons, which were located in the electron density maps and refined semi-free using distance restraints appropriate for 100 K. Methyl group hydrogen atoms were handled on a case-by-case basis. When maxima for methyl group hydrogen atoms could be observed in the electron density, the torsion angle was determined by a difference Fourier analysis followed by a rigid group refinement. In other cases, the methyl groups were modeled to an idealized disordered methyl group, with two sets of hydrogen atoms at 50% occupancy, rotated relative to each other by 60°. The hydrogen atom isotropic displacement parameters were fixed to 1.5 (methyl) or 1.2 (non-methyl) times the *U* value of the atom to which they are bound. Distance similarity restraints and anisotropic displacement parameter restraints were placed on disordered atoms. Data collection and refinement parameters, and other details of refinement for individual structures can be found

in the Supporting Information (SI). Ellipsoid plots and other X-ray structure graphics were generated with Mercury CSD 3.3.

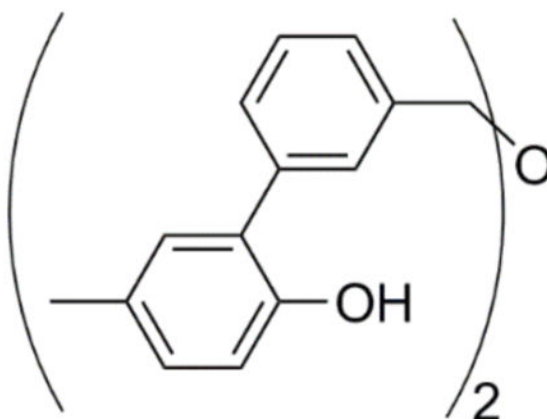
Synthesis

Ligand Synthesis

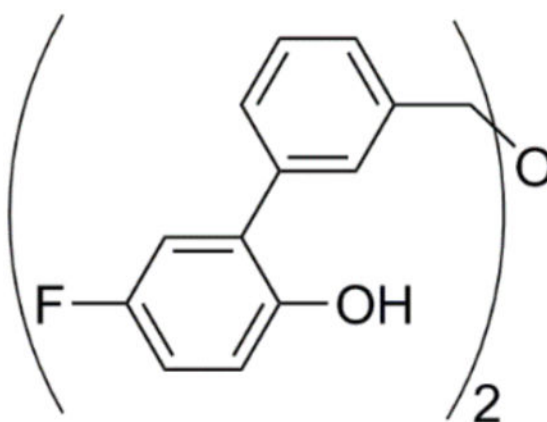
Bis(3-bromobenzyl)ether (L1): 3-Bromobenzaldehyde (9.25 g, 50 mmol) was added to 50 mL CH₂Cl₂ and afterwards triethylsilane (6.4 g, 55 mmol) was added. The reaction was cooled with an ice-bath at 0 °C. Triflic acid (44 μL) was added carefully to the solution. After 10 min stirring, the volume was reduced to about 20 mL and the solution was directly loaded onto a column of silica with some bicarbonate mixed in the top sand layer to remove trace acid. The product was eluted with hexanes to 2% ethyl acetate in hexanes. The combined fractions were stripped to form a colorless oil (7.8 g, 87.6%). Spectroscopic data matched that previously reported.¹⁶ An ~7% impurity of TES protected benzyl alcohol was present and easily removed during purification in the next synthetic step.



3',3'''-(Oxybis(methylene))bis(5-methyl-[1,1'-biphenyl]-2-ol) (L3a): L1 (2.98 g, 8.36 mmol), [Pd(PPh₃)₄] (386 mg, 334 μmol), (2-hydroxy-5-methylphenyl)boronic acid (3.18 g, 20.9 mmol), and K₃PO₄ (6.21 g, 29.3 mmol) were added to a Schlenk flask, placed under vacuum, and back-filled three times with nitrogen. Degassed water (30 mL) and THF (30 mL) were transferred into the flask via a cannula. The reaction was heated to 80 °C for 18 h before cooling to rt and subsequent quenching with 30 mL 1 M HCl (aq). The product was extracted with 3 × 50 mL ethyl acetate, dried over Na₂SO₄, filtered, and stripped to form an oil. Purification was achieved with column chromatography (hexanes to 20% ethyl acetate in hexanes), yielding L3a as a yellow solid (2.51 g, 73.0%). Spectroscopic data matched that previously reported.¹⁶

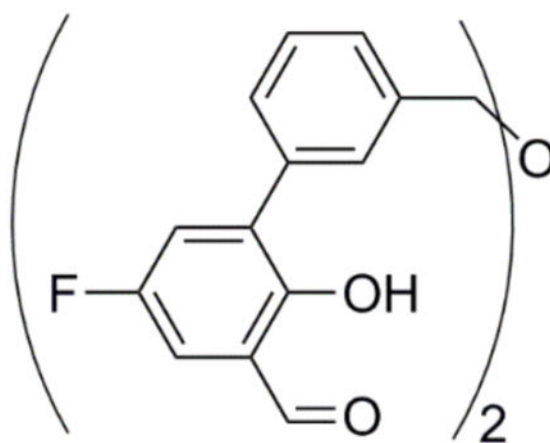


3',3'''-(Oxybis(methylene))bis(5-fluoro-[1,1'-biphenyl]-2-ol) (L3b): [Pd(PPh₃)₄] (175 mg, 385 μmol), (2-hydroxy-5-fluorophenyl)boronic acid (1.50 g, 9.62 mmol), and K₃PO₄ (2.87 g, 13.5 mmol) were added to a Schlenk flask. The system was placed under vacuum and back-filled with nitrogen three times. Degassed water (15 mL) and di(3-bromobenzyl) ether (1.37 g, 3.85 mmol) dissolved in THF (15 mL) were transferred into the flask by cannula. The system was heated to reflux and was allowed to stir for 20 h. Water (10 mL) was added and the product was extracted three times with 50 mL of ethyl acetate. The combined organic solutions were dried with MgSO₄, filtered, and stripped to form a black oil. Column chromatography (hexanes to 20% ethyl acetate in hexanes) yielded **L3b** as a tan solid (1.27 g, 78.5%). ¹H-NMR (CDCl₃, 500 MHz): δ 7.47 (m, 4H), 7.40 (m, 4H), 6.94 (m, 4H), 6.89 (m, 2H) 5.15 (br s, 1H), 4.65 (s, 4H). ¹³C-NMR (CDCl₃, 75 MHz): δ 157.23 (¹J_{C-F} = 239 Hz), 148.70 (⁴J_{C-F} = 2 Hz), 139.28, 136.79 (⁴J_{C-F} = 2 Hz), 129.63, 129.12 (³J_{C-F} = 8 Hz), 128.65, 128.59, 127.86, 117.12 (³J_{C-F} = 8 Hz), 116.65 (²J_{C-F} = 23 Hz), 115.63 (²J_{C-F} = 23 Hz), 72.52. ¹⁹F-NMR (CDCl₃, 282 MHz): δ -124.3 (m). Mp = 86 °C.

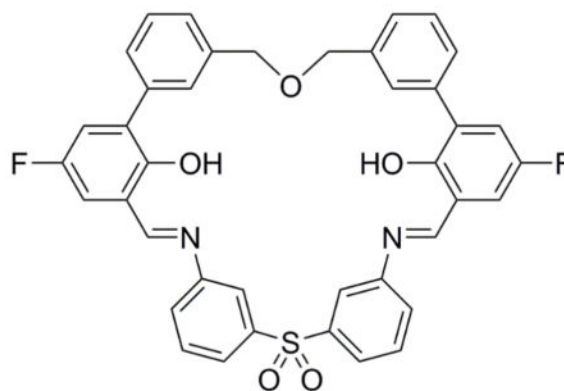


3',3'''-(Oxybis(methylene))bis(5-fluoro-2-hydroxy-[1,1'-biphenyl]-3-carbaldehyde) (L4b): This reaction is extremely moisture sensitive and it is therefore important to rigorously dry all reagents and solvents. **L3b** (1.13 g, 2.70 mmol), paraformaldehyde (1.22 g, 40.5 mmol), MgCl₂ (1.03 g, 10.8 mmol), and TEA (2.26 mL, 16.2 mmol) were added to a

Schlenk flask containing 7.5 g of 3 Å activated sieves. Acetonitrile (125 mL) was added to the flask by cannula. The reaction mixture was heated to reflux and stirred for 3 days, quenched with 1 M HCl (ca. 125 mL), and stripped from as much acetonitrile as possible. The product was extracted with 3 × 150 mL of ethyl acetate. The combined organic layers were dried with Na₂SO₄, filtered, and stripped to afford a dark green oil. Purification by column chromatography (hexanes to 10% ethyl acetate in hexane) yielded **L4b** as a light yellow solid (410.4 mg, 32.1%). ¹H-NMR (CDCl₃, 500 MHz): δ 11.34 (s, 2H), 9.86 (s, 2H), 7.62 (s, 2H), 7.53 (d, 2H), 7.45 (m, 4H), 7.37 (dd, 2H), 7.24 (dd, 2H), 4.67 (s, 4H). ¹³C-NMR (CDCl₃, 125 MHz): δ 195.85, 155.58 (¹J_{C-F} = 240 Hz), 155.31 (⁴J_{C-F} = 2 Hz), 138.52, 135.48 (⁴J_{C-F} = 1 Hz), 132.23 (³J_{C-F} = 7 Hz), 128.62, 128.60, 127.68, 125.14 (²J_{C-F} = 24 Hz), 120.42 (³J_{C-F} = 6 Hz), 117.35 (²J_{C-F} = 22 Hz), 72.15. ¹⁹F-NMR (CDCl₃, 282 MHz): δ -123.7 (t, ³J_{H-F} = 8 Hz). ESI-MS(-) = 473.1 [M-H]⁻ (Calcd = 473.12 [M-H]⁻), ESI-MS(+) = 513.1 [M+K]⁺, (Calcd = 513.09 [M+K]⁺). Mp = 123 °C.



H₂F₂PIM: 3,3'-Diaminodiphenyl sulfone (196 mg, 790 μmol) and **5b** (375 mg, 790 μmol) were added to a dry Schlenk flask with 175 mL of dry acetonitrile. Trifluoroacetic acid (220 μL) was added to the mixture, which was heated to 85 °C. After 6 h, the reaction was allowed to cool to rt, during which time a large amount of yellow precipitate formed. The solid was collected by filtration, washed with ether, and dried under vacuum. The material (382 mg, 70.4%) was used without further purification. ¹H-NMR (CDCl₃, 500 MHz): δ 13.18 (br s, 1H), 8.62 (s, 2H), 7.92 (d, 2H), 7.83 (s, 2H), 7.76 (s, 2H), 7.59 (t, 2H), 7.44 (m, 6H), 7.36 (d, 2H), 7.22 (dd, 2H), 7.12 (dd, 2H), 4.68 (s, 4H). ¹³C-NMR (CD₂Cl₂, 125 MHz): δ 164.35, 156.06 (¹J_{C-F} = 237 Hz), 155.60, 149.69, 143.64, 138.52, 137.33, 132.19 (³J_{C-F} = 7 Hz), 131.46, 130.21, 129.41, 128.84, 128.63, 126.38, 124.95, 123.56, 122.19 (²J_{C-F} = 24 Hz), 119.52 (³J_{C-F} = 8 Hz), 117.37 (²J_{C-F} = 23 Hz), 74.07. ¹⁹F-NMR (CD₂Cl₂, 470 MHz): δ -125.6 (t, ³J_{H-F} = 9 Hz). Mp = 184 °C.



Metal Complex Synthesis

[Fe₂(PIM)(Ar^{4F-Ph}CO₂)₂] (10): H₂PIM (157.5 mg, 232 μmol) and Ar^{4F-Ph}CO₂H (144.0 mg, 463 μmol) were combined in 3 mL of THF. [Fe₂(mes)₄] (136.5 mg, 232 μmol), pre-dissolved in 1.5 mL THF, was injected quickly to create a dark red mixture. After 3 h, the solvent was stripped, the crude residue washed with 3 × 1 mL ether, and the material was crystallized by slow diffusion of pentane into a solution in CH₂Cl₂. The resulting red crystals were washed (2 × 1 mL pentane) and dried under vacuum to yield 242.2 mg, 74.2% red crystalline material. Anal. Calcd for Fe₂C₈₀H₅₄F₄N₂O₉S·(C_{0.5}H₁Cl₁) (**10**·0.5CH₂Cl₂): C, 66.70; H, 3.82; N, 1.93. Found: C, 66.95; H, 3.61; N, 1.92. CH₂Cl₂ was detected in solution NMR samples of **10** in THF-*d*₈. IR (KBr): 3049, 2920, 2850, 2336, 1653, 1604, 1573, 1534, 1506, 1433, 1411, 1382, 1325, 1308, 1282, 1221, 1199, 1091, 1074, 979, 837, 790, 707, 685, 595, 539, and 469 cm⁻¹. Mössbauer (polycrystalline, apiezon M grease): δ = 1.05(2) mm/s, E_Q = 2.12(2) mm/s, Γ_{L/R} = 0.33(2) mm/s. Mp (dec) = 74 °C.

[Fe₂(F₂PIM)(Ar^{Tol}CO₂)₂] (11): H₂F₂PIM (150 mg, 218 μmol) and Ar^{Tol}CO₂H (132 mg, 437 μmol) were dissolved in THF (3 mL) in a dry box. [Fe₂(mes)₄] (129 mg, 218 μmol) was dissolved in 1.5 mL THF and added to the mixture. After 2 h, the solvent was removed and the residue washed twice with 1 mL of ether. The residue was then dissolved in 2 mL of CH₂Cl₂ and layered with 10 mL of pentane. The resultant material (278 mg, 91.0%) was filtered and washed with pentane. X-ray quality crystals were obtained by slow diffusion of pentane into a solution of **11** in CH₂Cl₂. Anal. Calcd for Fe₂C₈₂H₆₀F₂N₂O₉S·(C₄H₉Cl₃) (**11**·1.5CH₂Cl₂·0.5C₅H₁₂): C, 66.10; H, 4.45; N, 1.79. Found: C, 66.18; H, 4.06; N, 1.82. CH₂Cl₂ and pentane were detected in NMR samples of **11**. IR (KBr): 3054, 3028, 2915, 2857, 1649, 1601, 1581, 1527, 1449, 1434, 1403, 1386, 1341, 1302, 1277, 1201, 1184, 1149, 1110, 1070, 1000, 956, 881, 838, 762, 736, 702, 685, 604, 543, 529, and 459 cm⁻¹. Mössbauer (polycrystalline, apiezon M grease): (site 1, 50%): δ = 0.93(2) mm/s, E_Q = 2.03(2) mm/s, Γ_{L/R} = 0.27(2) mm/s (site 2, 50%): δ = 1.15(2) mm/s, E_Q = 1.98(2) mm/s, Γ_{L/R} = 0.28(2) mm/s. Mp (dec) = 200 °C.

[Fe₂(F₂PIM)(Ar^{4-Ph}CO₂)₂] (12): The same procedure was used as that described for **10** except that H₂F₂PIM (159 mg, 232 μmol) replaced H₂PIM. Obtained were 304.7 mg, 92.8% of maroon crystals. Anal. Calcd for Fe₂C₇₈H₄₈F₂N₂O₉S·(CH₂Cl₂) (**12**·CH₂Cl₂): C, 63.00; H, 3.31; N, 1.81. Found: C, 63.26; H, 3.36; N, 1.87. CH₂Cl₂ was detected in NMR samples

of **12**. IR (KBr): 3054, 2954, 2933, 2859, 1610, 1581, 1532, 1510, 1446, 1405, 1386, 1321, 1299, 1212, 1187, 1152, 1074, 1001, 958, 840, 794, 698, 633, 542, and 469 cm⁻¹. Mössbauer (polycrystalline, apiezon M grease): $\delta = 1.04(2)$ mm/s, $E_Q = 2.01(2)$ mm/s, $\Gamma_{L/R} = 0.33(2)$ mm/s. Mp (dec) = 232 °C.

Results and Discussion

Synthesis and Characterization

In our previous report, H₂PIM was prepared in gram quantities by an 8 step synthesis.¹⁶ Since then, a shorter route with 5 steps was developed (Scheme 3). Instead of the original two-step procedure to produce the bis(3-bromobenzyl)ether (**L1**), a reductive condensation reaction²⁵ was utilized with 3-bromobenzaldehyde, 1.1 equiv of Et₃SiH, and 1 mol% TfOH. After 10 min of reaction time, immediate purification provides gram quantities of **L1** in 87.6% yield. The original synthesis of H₂PIM (Scheme S1) was limited by a Negishi-coupling of **L1** and the aryl-zinc reagent of 2-bromo-4-methyl-phenol-tetrahydropyran that proceeded in 35% yield.¹⁶ To improve this coupling step, the aryl-zinc reagent was replaced with an aryl-boronic acid, **L2**, to do a Suzuki-coupling. By doing so, a protecting group for the phenoxy moiety was not needed, eliminating the next step in the main synthetic sequence. Thus, the new synthesis required (2-hydroxy-5-methylphenyl)boronic acid (**L2a**), which was prepared from the commercially available (2-methoxy-5-methylphenyl)boronic acid following a literature procedure.¹⁸ The Suzuki-coupling between **L1** and **L2a** yielded the desired product, **L3a**, in 61–80% yield using [Pd(PPh₃)₄] as the catalyst. The last step of the synthesis was unmodified. In total, the overall yield for the synthesis of H₂PIM increased to 30.9% from 13.3%. H₂F₂PIM, the analogue of H₂PIM where fluorine substituents replace the methyl groups, was prepared in an analogous manner in an overall yield of 15.1%. The solid-state structures of both H₂PIM and H₂F₂PIM were obtained and show the ligands to be preorganized for supporting a dinuclear complex. Crystallographic details are reported in the Supporting Information (SI).

Analogous to the synthesis of **1-2**, **10-12** were synthesized in one pot by mixing the appropriate macrocyclic ligand, 2.0 equiv of carboxylic acid, and 1.0 equiv of [Fe₂(mes)₄] in THF; the yields ranged from 74.2–92.8%. X-ray quality crystals of **10-12** were obtained by slow diffusion of pentane into methylene chloride solutions of the complexes (Figure 2). Compounds **10-12** feature the expected syn-*N* dicarboxylate-bridged diiron centers. A comparison of the bond distances in the *m*-terphenylcarboxylate-bridged complexes **2** and **10-12** is provided in Table 1. There are noteworthy differences in bond distances and angles of the μ - η^1 : η^2 bridging carboxylate ligand for these structures. The Fe₁—O₃ bond length increases from 2.342(6) Å in **2** to 2.348(2) Å in **12**, 2.443(2) Å in **11**, and 2.535(2) Å in **10**. The trend does not follow the number of methyl-to-fluoro substitutions in the complexes and is tentatively attributed to packing interactions. The weakening of the Fe1—O3 interaction correlates with an increase in the Fe1—O4—C1 angle, which rises from 95 ° in **2** and **12** to 99 ° in **11** and 102 ° in **10**. A corresponding decrease in the Fe1—O4 distance occurs, from 2.103(2) Å in **12** to 2.062(2) Å in **11** and 2.043(2) Å in **10**. These correlated changes are consistent with what is predicted to occur for varying the strength of the interaction of the

dangling oxygen to the metal center⁹ and demonstrate a minor carboxylate shift within the solid state.

In all solid-state structures to date containing PIM or F₂PIM there is a wedge-shaped conformation (curved green line, Figure S14). In **2** and **10-12**, the wedge provides space for the *m*-terphenyl group of the μ - η^1 : η^2 bridging carboxylate, which packs along the walls of the wedge (Figure S15). The *m*-terphenyl unit of the μ - η^1 : η^1 bridging carboxylate is oriented perpendicular to the edge of the wedge (Figure S15). The configuration in **1** (Figure S15, top left) is reversed, however, most likely as a consequence of the shape of the carboxylate. The steric bulk of the trityl groups in **1** is directed away from the macrocycle whereas the *m*-terphenyl groups in the other complexes point toward the macrocycle. The *m*-terphenyl groups impose a stronger effect on the conformation of the macrocycle. These points will be important later in our discussion of the solution dynamics of these complexes.

Mössbauer spectra for compounds **10-12** were obtained at 80 K and compared to those for **1** and **2** (Table 2). Compounds **1-2** and **11** nicely fit to a two-site model and **10** and **12** fit to a single site (Figure 3 and S6). The reason for the difference is not clear, although **10** and **12** both contain the Ar^{4F-Ph}CO₂H carboxylate, unlike the carboxylates in **1** (Ph₃CCO₂H) and **2** and **11** (Ar^{Tol}CO₂H). The δ values for **10-12** range from 0.93 to 1.15 mm/s with E_Q values ranging from 1.98 to 2.12 mm/s, consistent with high-spin Fe(II) centers, as is the case with **1-2**.

NMR Studies

Owing to the rare asymmetric carboxylate bridging modes in **1-2** as well as the importance of the carboxylate shift in BMMs, we sought to understand the carboxylate dynamics in this system by using solution NMR spectroscopy. Standard ¹H spectroscopic NMR techniques were not possible because of paramagnetic effects, but fluorine substitutions provide a spectroscopic handle with ¹⁹F NMR. VT ¹⁹F NMR spectra for **10-12** were obtained.

In THF-*d*₈, the ¹⁹F NMR spectrum of compound **10** shows a single fluorine peak at -116 ppm, indicating rapid exchange of all four F atoms at room temperature. As the system is cooled down, the single peak remains and broadens slightly upon reaching -70 °C. The broadening suggests that fluorine atom exchange was slowed down, but not enough to show splitting on the ¹⁹F NMR timescale. We wondered whether the coordinating capabilities of THF to the iron atoms may increase the exchange rates of the carboxylate ligands, and CD₂Cl₂ was therefore investigated as an alternative solvent.

At 35 °C in CD₂Cl₂, **10** displays a single ¹⁹F peak at -113.9 ppm. As the temperature is decreased, this peak broadens and becomes nearly flat at -10 °C (Figure 4). Two peaks then grow in at -109.0 ppm and -119.2 ppm, commencing at -20 °C. The feature at -109.0 ppm sharpens into a peak at -106.3 ppm at -60 °C and then starts to broaden and further shift to -103.4 ppm at -95 °C, possibly due to increased solvent viscosity at low temperature. The peak at -119.2 ppm sharpens slightly at -30 °C and shifts to -120.3 ppm and then broadens into the background at -50 °C. After further cooling to -60 °C, two peaks arise at -118.2 ppm and -127.8 ppm, which sharpen and shift to -119.3 ppm and -131.3 ppm at -80 °C before broadening at -95 °C with chemical shift values of -120.6 and -134.4 ppm.

Integration of the three peaks (−104.6, −119.3, and −131.3 ppm) at −80 °C reveals a ratio of 2:1:1, respectively. We refer to the first peak split at 35 °C at −113.9 ppm as process 1 and the split of the broad −120.3 ppm peak at −30 °C as process 2. At 35 °C and below, four very weak fluorine resonances of unknown origin were observed at −111.6, −112.2, −113.1, and −119.5 ppm. These features are believed to be associated with a structurally similar species and are also observed in samples of **2+10** and **12**, discussed below.

To test whether the dynamic processes observed for **10** occur through intermolecular or intramolecular exchange events, we prepared a mixture of **2** and **10** and repeated the ^{19}F NMR experiment. If intermolecular exchange of carboxylates occurs, a new species with a mixture of carboxylates, $[\text{Fe}_2(\text{PIM})(\text{Ar}^{\text{Tol}}\text{CO}_2)(\text{Ar}^{4\text{F-Ph}}\text{CO}_2)]$, would form, which might be distinguishable from **10** by its ^{19}F NMR spectrum (Scheme 4). At 35 °C, two fluorine peaks are observed at −113.0 and −113.9 ppm (Figure S1), a clear indication that intermolecular carboxylate exchange occurs. Furthermore, the observation of two, instead of one, peak means that the intermolecular carboxylate exchange process is slower on the NMR time scale at 35 °C. Therefore, all exchange processes that we observe in our VT experiments in CD_2Cl_2 are intramolecular processes. To ensure that the exchange processes observed in the VT NMR of **10** were not altered by addition of **2**, the spectrum was examined down to −95 °C. The VT NMR of **2+10** looks the same as that as **10** alone except that the number of peaks is doubled owing to the presence of $[\text{Fe}_2(\text{PIM})(\text{Ar}^{\text{Tol}}\text{CO}_2)(\text{Ar}^{4\text{F-Ph}}\text{CO}_2)]$. At −50 °C, an additional peak occurs at −107.0 ppm and at −80 °C, and additional peaks are observed at −120.1 and −135.2 ppm. Integration at −80 °C, however, reveals an approximately 4:1:1 ratio in order of decreasing chemical shift. This observation suggests that the two carboxylate positional isomers of $[\text{Fe}_2(\text{PIM})(\text{Ar}^{\text{Tol}}\text{CO}_2)(\text{Ar}^{4\text{F-Ph}}\text{CO}_2)]$ are not equivalent and that one is favored over the other. This ratio also supports the notion that process 1 involves an exchange between the two carboxylate positions.

Having asymmetric bridging carboxylates in these diiron(II) complexes eliminates the 2-fold symmetry axis of the $\text{X}_2\text{PIM}^{2-}$ ligand and introduces chirality to these complexes. Moreover, the two fluorine atoms in $\text{F}_2\text{PIM}^{2-}$ are chemically inequivalent in these complexes and could offer some information about the intramolecular exchange processes observed in **10**. To explore this possibility, we first examined the VT ^{19}F NMR spectrum of **11** in CD_2Cl_2 . At 35 °C, a single fluorine resonance occurs at −32.4 ppm (Figure S2). The free ligand, $\text{H}_2\text{F}_2\text{PIM}$, has a fluorine chemical shift at −125.6 ppm in CD_2Cl_2 at 25 °C. The 93 ppm difference in chemical shift is indicative of paramagnetic shifting and proves that iron binds to $\text{F}_2\text{PIM}^{2-}$ in solution. Cooling to −95 °C shifts the −32.4 ppm resonance to 38.8 ppm. The peak slowly broadens with decreasing temperature, indicating that the two fluorine atoms exchange rapidly on the NMR time scale at all temperatures in this experiment, but the broadening at low temperature suggests that the exchange process slows down. Another possibility is that the broadening is due to viscosity changes as the temperature is lowered. The chemical shift change in this fluorine peak follows Curie behavior (Figure S3).

The VT ^{19}F NMR spectrum of **12** was also obtained to ensure that the change to $\text{F}_2\text{PIM}^{2-}$ from PIM^{2-} does not alter the exchange processes observed in **10**. Indeed, no significant changes occurred for **12** except for slight alterations in chemical shifts (Figure S4). The

F_2PIM^{2-} fluorine resonance in **12** is 1.6–6.5 ppm upfield relative to that in **11**. The $Ar^{4F-Ph}CO_2^-$ fluorine resonances in **12** are 1.2–3.2 ppm upfield of those in **10**. We can conclude that there are no significant differences between in the exchange processes in complexes **2** and **10-12**.

A model for these intermolecular processes is presented in Scheme 5. The PIM fluorine substituents are labeled A or B and each fluorine atom on the carboxylate ligands is assigned the color blue, orange, green, or red. Examination of the space filling model of any of the complexes **2** and **10-12** clearly indicates that rotation of the $\mu-\eta^1:\eta^2$ carboxylate would be unlikely due to a steric clash with the PIM macrocycle. Rotation of the $\mu-\eta^1:\eta^1$ carboxylate to interchange the blue and orange markers appears possible, although one of the two Fe-O bonds might need to transiently dissociate in the process. The $\mu-\eta^1:\eta^2$ carboxylate could shift into a $\mu-\eta^1:\eta^1$ bridging mode to form an intermediate with approximate two-fold symmetry. If the same carboxylate undergoes a $\mu-\eta^1:\eta^1$ to $\mu-\eta^1:\eta^2$ carboxylate shift, it would either return to the original complex or the mirror image of the original complex. The mirror image results in the interchange of A and B. Similar to the blue and orange carboxylates, the green and red carboxylates may be able to rotate in a $\mu-\eta^1:\eta^1$ bridging mode and such green-red intramolecular interchange could occur after a $\mu-\eta^1:\eta^1$ to $\mu-\eta^1:\eta^2$ carboxylate shift. As discussed above, the PIM and F_2PIM macrocycles in **2** and **10-12** adopt a wedge-shaped conformation that encircles the diiron(II) center. The diphenylsulfone unit curves to orient the wedge-shape to form a cradle for the *m*-terphenyl group of the $\mu-\eta^1:\eta^2$ bridging carboxylate. In order to interchange the blue/orange and red/green pairs (Scheme 5), the macrocyclic ligand must undergo a conformational change that inverts the conformation of the sulfone, hereafter the “sulfone inversion.” With the *m*-terphenyl group of the $\mu-\eta^1:\eta^2$ bridging carboxylate packed tightly with the macrocyclic cradle, it is likely that a carboxylate shift to the symmetric intermediate would be necessary before a sulfone inversion, which would need to be associated with rotations of both carboxylates. The sulfone inversion would lead to mixing of all color markers and A and B.

From the VT NMR spectroscopic experiments, we know that process 1 distinguishes the two carboxylates, which corresponds to the sulfone inversion in our model. Process 2 differentiates the two sides of either the red/green or the blue/orange carboxylates (Scheme 5). Our data do not allow us to conclusively assign the individual carboxylates in this exchange process. A blue/orange exchange by rotation of the O_2C-C_{aryl} bond appears to be sterically inhibited by sulfone and ether units of the macrocycle projecting below the macrocycle plane. A similar O_2C-C_{aryl} bond rotation on the red/green carboxylate on the canyon side of the macrocycle during a $\mu-\eta^1:\eta^1$ bridging mode intermediate appears less sterically hindered than that of the blue/orange exchange. We therefore tentatively assign process 2 as a blue/orange exchange. The carboxylate exchange that gives rise to process 2 slows down sufficiently below $-95^\circ C$ to give rise to the observed NMR spectral behavior, characterized by broadened peaks at -103.4 and -104.9 ppm in **10** and **12**, respectively. Additional broadening occurs below $-80^\circ C$ for the upfield carboxylate at -119.3 and -131.3 ppm in **10** and may reflect hindered rotation of the 4-fluorophenyl groups on the *m*-terphenyl groups of the $Ar^{4F-Ph}CO_2^-$ ligand. The data from the macrocycle fluorine atoms in

11 and **12** are consistent with interconversion of the two enantiomers generated by the carboxylate shift remaining rapid on the NMR time scale even at $-95\text{ }^{\circ}\text{C}$.

Comparison to MMOH

A significant change in the coordination mode of the bridging Glu243 in MMOH occurs upon reduction of the diiron(III) active site to the diiron(II) form.³ EXAFS²⁶ and MCD²⁷ studies of MMOH_{red} in complex with the regulatory protein, MMOB, showed additional alterations in the primary coordination sphere at the diiron center at the active site. The MCD study suggested coordination changes in Glu209 to be the main alteration. A comparison of diiron active sites in X-ray structures of MMOH_{red} and that of the H-B complex reveal that, in both cases, Glu243 bridges in a $\mu\text{-}\eta^1\text{:}\eta^2$ mode, but the conformation differs.²⁸ The 2.9 Å resolution of the latter complex as well as the ambiguity of its oxidation state prevent a meaningful explanation, however. Nevertheless, it is clear from all these observations that there is conformational flexibility in the coordination of Glu209 and Glu243 at the active site of MMOH_{red}. In the present model system, the macrocyclic framework preorganizes the diiron(II) center to contain both $\mu\text{-}\eta^1\text{:}\eta^1$ and $\mu\text{-}\eta^1\text{:}\eta^2$ bridging modes, similar to that in MMOH_{red}. The variable temperature ¹⁹F solution NMR spectroscopic study described here demonstrates that the bridging carboxylates retain the ability to shift coordination modes while remaining as a diiron(II) complex. Thus the diiron(II) PIM complexes have the flexibility to accommodate structural changes, evoked by temperature changes, that provide a valuable precedent of potential relevance to the conformational alterations observed in soluble methane monooxygenase.

Conclusions

A series of fluorine substituted analogues of **2**, **10-12**, were prepared and characterized. From VT ¹⁹F NMR spectra of these complexes it was possible to characterize intramolecular carboxylate exchange processes for this family of syn-*N* asymmetrically carboxylate-bridged diiron(II) complexes. The results mimic the occurrence of carboxylate shifts observed in MMOH_{red}, evoked both by redox changes and complex formation with the regulatory protein MMOB.

Supplementary Material

Refer to Web version on PubMed Central for supplementary material.

Acknowledgments

This work was supported by a grant from the National Institute of General Medical Sciences (Grant GM 32114 to S. J. Lippard) and the National Science Foundation Graduate Research Fellowship Program (Grant No. 1122374 to M. A. Minier).

References

1. Feig AL, Lippard SJ. Chem Rev. 1994; 94:759–805.
2. Wallar BJ, Lipscomb JD. Chem Rev. 1996; 96:2625–2658. [PubMed: 11848839]
3. Merckx M, Kopp DA, Sazinsky MH, Blazyk JL, Müller J, Lippard SJ. Angew Chem Int Ed. 2001; 40:2782–2807.

4. Tinberg CE, Lippard SJ. *Acc Chem Res.* 2011; 44:280–288. [PubMed: 21391602]
5. Rosenzweig AC, Frederick CA, Lippard SJ, Nordlund P. *Nature.* 1993; 366:537–543. [PubMed: 8255292]
6. Rosenzweig AC, Lippard SJ. *Acc Chem Res.* 1994; 27:229–236.
7. Rosenzweig AC, Nordlund P, Takahara PM, Frederick CA, Lippard SJ. *Chem Biol.* 1995; 2:409–418.
8. Whittington DA, Lippard SJ. *J Am Chem Soc.* 2001; 123:827–838. [PubMed: 11456616]
9. Rardin RL, Tolman WB, Lippard SJ. *New J Chem.* 1991; 15:417–430.
10. Do LH, Hayashi T, Moëne-Loccoz P, Lippard SJ. *J Am Chem Soc.* 2010; 132:1273–1275. [PubMed: 20055391]
11. Frisch JR, McDonnell R, Rybak-Akimova EV, Que L. *Inorg Chem.* 2013; 52:2627–2636. [PubMed: 23432330]
12. Que L, Tolman WB. *Nature.* 2008; 455:333–340. [PubMed: 18800132]
13. Do LH, Lippard SJ. *J Inorg Biochem.* 2011; 105:1774–1785. [PubMed: 22113107]
14. Burger B, Dechert S, Gro Demeshko S, Meyer F. *Chem Commun.* 2011; 47:10428–10430.
15. Lee D, Lippard SJ. *Inorg Chem.* 2002; 41:2704–2719. [PubMed: 12005495]
16. Do LH, Lippard SJ. *J Am Chem Soc.* 2011; 133:10568–10581. [PubMed: 21682286]
17. Chen CT, Siegel JS. *J Am Chem Soc.* 1994; 116:5959–5960.
18. Vishnumurthy K, Makriyannis A. *J Comb Chem.* 2010; 12:664–669. [PubMed: 20831265]
19. APEX2. APEX2, 2008–4.0. Bruker AXS, Inc; Madison, WI: 2008.
20. SAINT. SAINT: SAX Area-Detector Integration Program, 2008/1. University of Göttingen; Göttingen, Germany: 2008.
21. Sheldrick, GM. SADABS: Area-Detector Absorption Correction. University of Göttingen; Göttingen, Germany: 2008.
22. XPREP. XPREP, 2008/2. Bruker AXS; Madison, WI: 2008.
23. Sheldrick G. *Acta Cryst Sec A.* 2008; 64:112–122.
24. Spek, AL. PLATON, A Multipurpose Crystallographic Tool. Utrecht University; Utrecht, The Netherlands: 2008.
25. Gellert BA, Kahlcke N, Feurer M, Roth S. *Chem Eur J.* 2011; 17:12203–12209. [PubMed: 21922582]
26. Rudd DJ, Sazinsky MH, Lippard SJ, Hedman B, Hodgson KO. *Inorg Chem.* 2005; 44:4546–4554. [PubMed: 15962961]
27. Miti N, Schwartz JK, Brazeau BJ, Lipscomb JD, Solomon EI. *Biochemistry.* 2008; 47:8386–8397. [PubMed: 18627173]
28. Lee SJ, McCormick MS, Lippard SJ, Cho US. *Nature.* 2013; 494:380–384. [PubMed: 23395959]

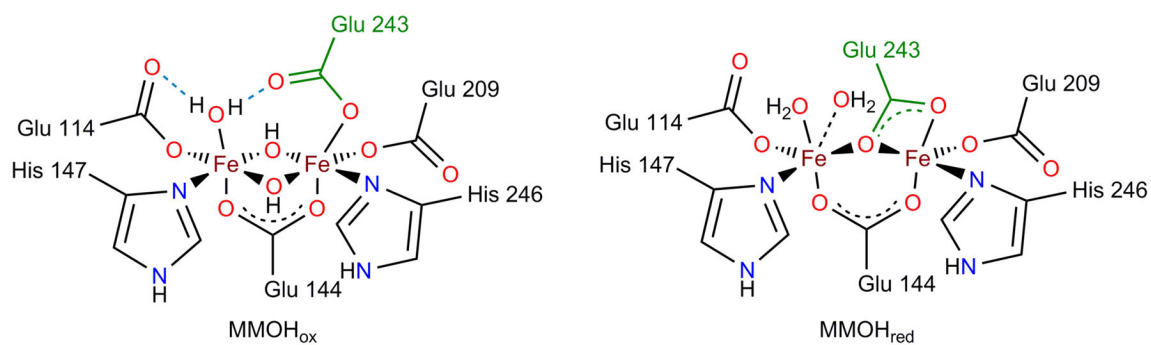


Figure 1. Graphical representations of the oxidized (left) and reduced (right) MMOH active sites. The green coloring highlights a carboxylate shift in Glu243 between the two structures.

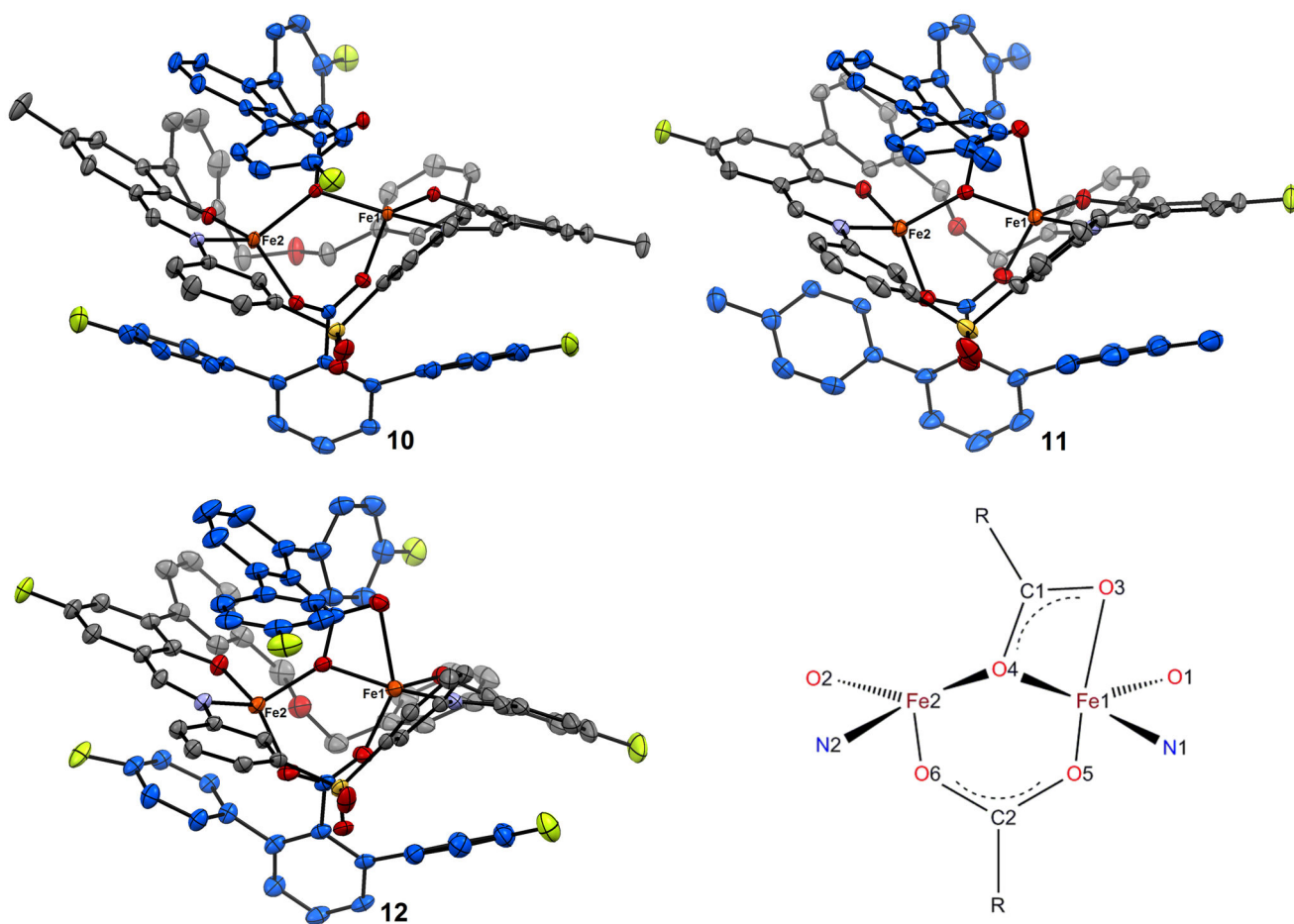


Figure 2. Solid state structures of **10-12** and cartoon of the $\mu\text{-}\eta^1:\eta^2$ carboxylate bridging mode (bottom right). Ellipsoids are drawn at 50% and solvents, disordered atoms, and hydrogen atoms are removed for clarity. The carbon atoms of the *m*-terphenyl wings are colored bright blue to help distinguish those atoms from that of the macrocyclic ligand.

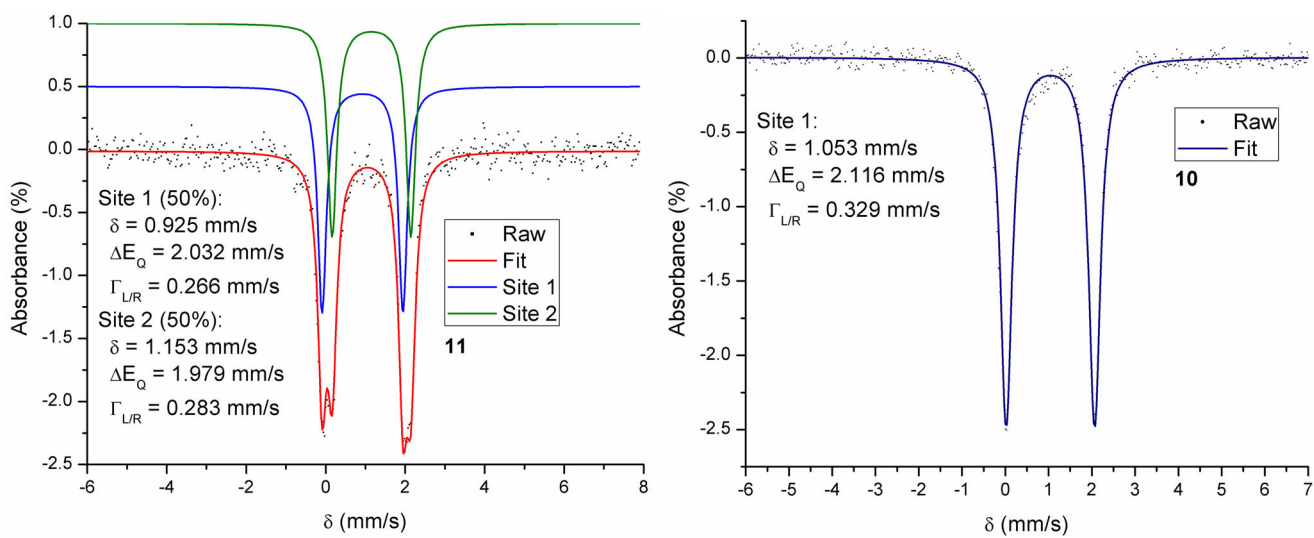


Figure 3.
Mössbauer spectra of **11** (left) and **10** (right).

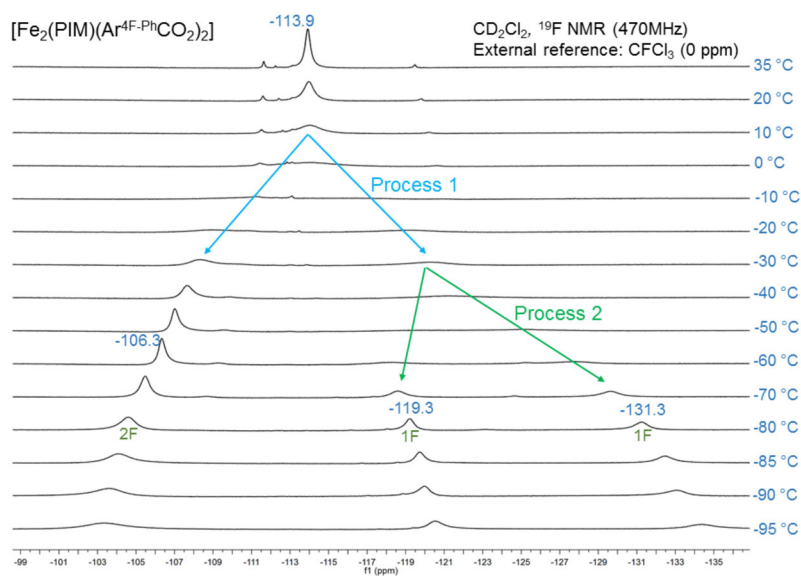
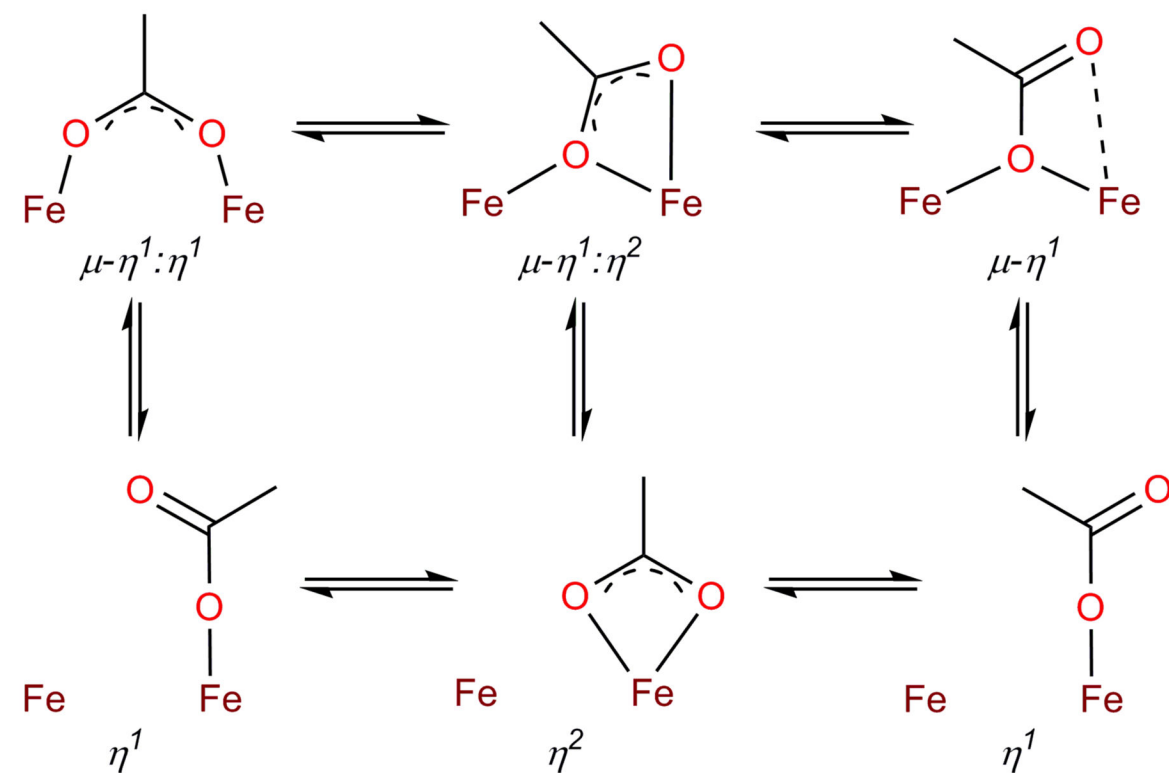
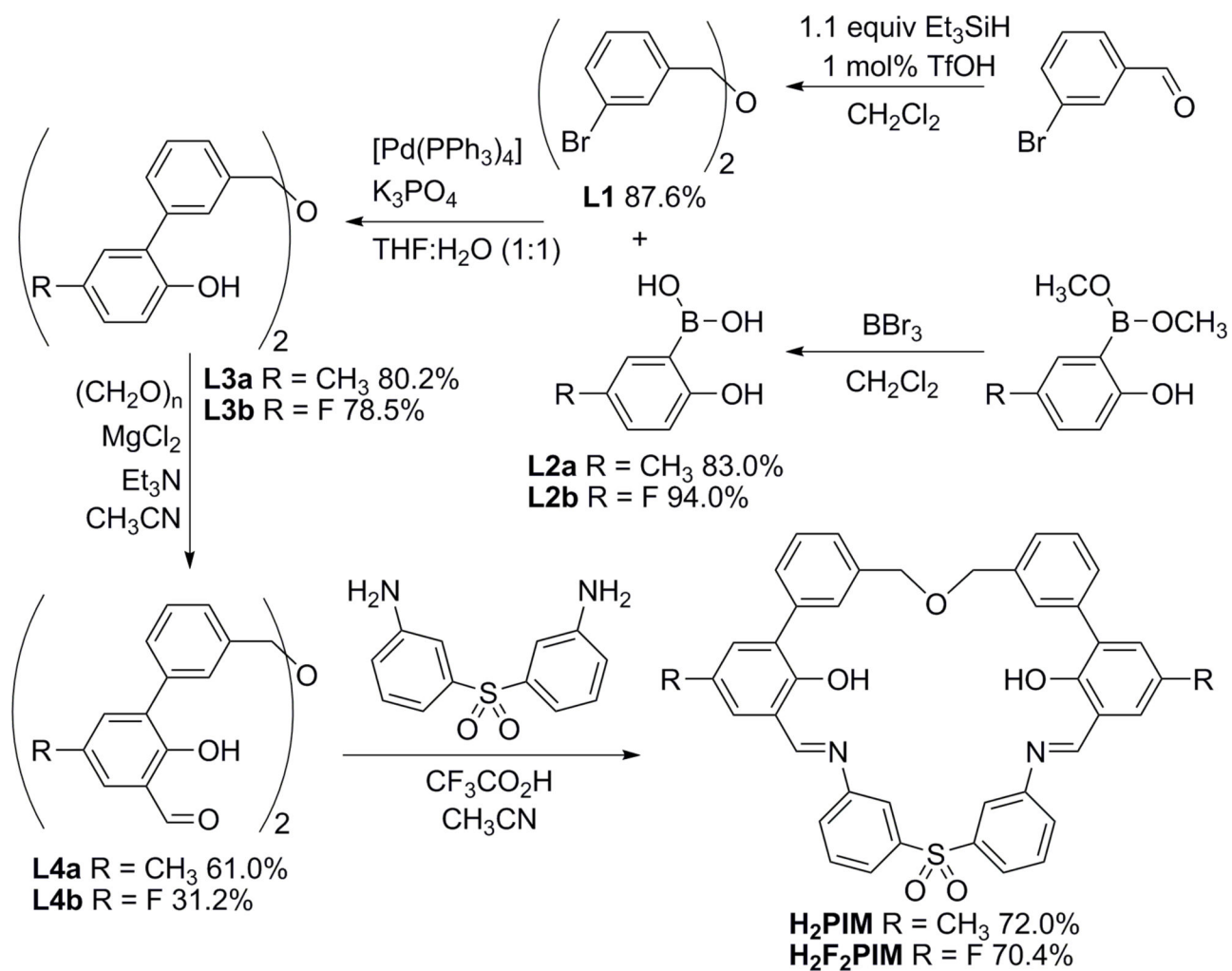


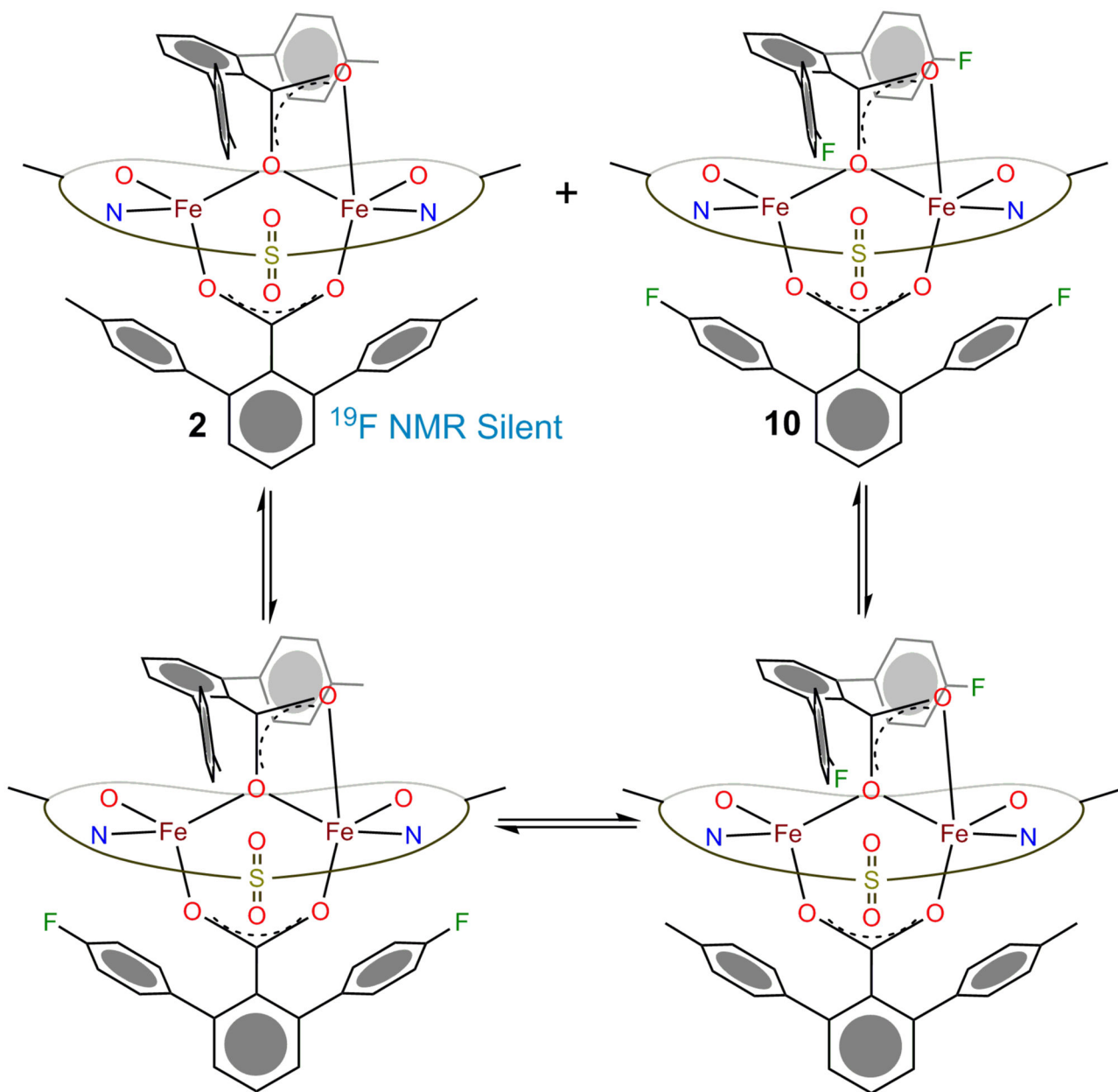
Figure 4. VT ¹⁹F NMR of **10** in CD₂Cl₂. Intramolecular processes 1 and 2 are highlighted in blue and green respectively. Minor impurities are observed at higher temperatures.



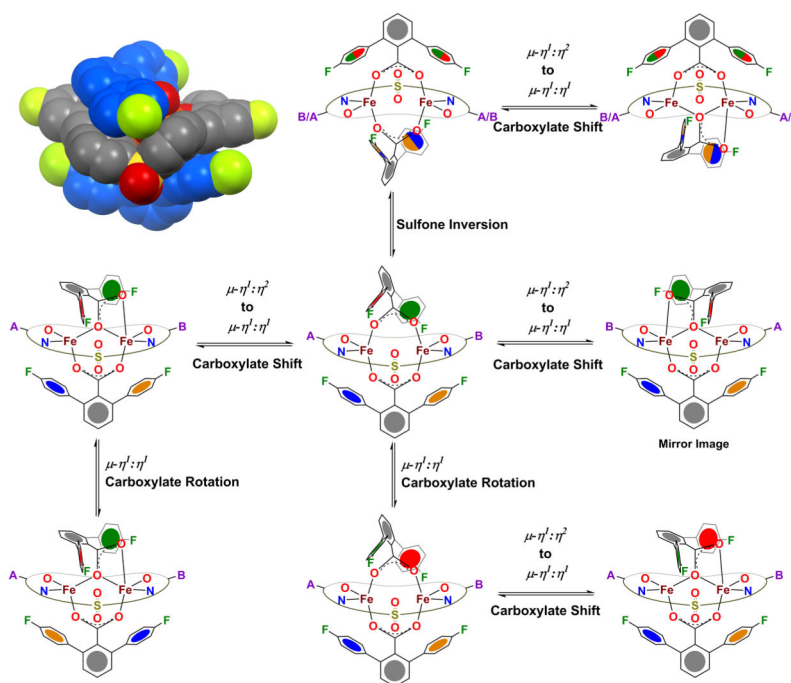
Scheme 1.
The carboxylate shift in diiron complexes.



Scheme 3.
 Synthesis of H_2PIM and $\text{H}_2\text{F}_2\text{PIM}$.

**Scheme 4.**

Depiction of the intermolecular carboxylate exchange between **2** and **10** through an intermediate, $[\text{Fe}_2(\text{PIM})(\text{Ar}^{\text{Tol}}\text{CO}_2)(\text{Ar}^{4\text{F-Ph}}\text{CO}_2)]$.

**Scheme 5.**

Model for the intramolecular exchange processes that occurs in the family of compounds **2**, **10-12**. A space-filling model of **12** is provided in the top left in order to visualize the spatial orientation of the ligands.

Table 1

Comparison of select interatomic distances and angles in **2**, and **10-12**, in order of increasing Fe1—O3 distance.

Å	Fe1-Fe2	Fe1-O1	Fe1-Ni	Fe1-O3	Fe1-O4	Fe1-O5	Fe2-O2	Fe2-N2	Fe2-O4	Fe2-O6
2	3.601(1)	1.895(4)	2.044(4)	2.342(6)	2.091(3)	2.048(6)	1.888(3)	2.038(5)	2.029(4)	1.998(4)
12	3.6387(6)	1.900(3)	2.054(3)	2.348(3)	2.103(2)	2.048(3)	1.888(3)	2.024(3)	2.039(2)	1.955(3)
11	3.5648(8)	1.883(3)	2.042(3)	2.443(2)	2.062(2)	2.028(2)	1.886(3)	2.031(3)	2.038(2)	1.991(2)
10	3.5680(7)	1.881(2)	2.051(3)	2.535(2)	2.043(2)	2.026(2)	1.877(2)	2.032(3)	2.055(2)	1.973(2)
°	Fe1-O4-Fe2	Fe1-O4-Cl	Fe2-O4-Cl							
2	122.2(2)	95.5(3)	133.4(4)							
12	122.9(1)	95.4(2)	133.8(2)							
11	120.8(1)	98.7(2)	129.9(2)							
10	121.0(1)	102.2(2)	132.9(2)							

Table 2

Mössbauer parameters for **1-2** and **10-12**.

(mm/s)	Site 1			Site 2				
	δ	E_Q	$\Gamma_{L/R}$	δ	E_Q	$\Gamma_{L/R}$		
1^a	0.97	2.25	0.35	47%	1.18	2.33	0.38	53%
2^a	0.95	2.02	0.32	37%	1.10	2.04	0.38	63%
11	0.93	2.03	0.27	50%	1.15	1.98	0.28	50%
10	1.05	2.12	0.33	---	---	---	---	---
12	1.04	2.01	0.33	---	---	---	---	---

^a Ref. 18.